Observing Electrochemical Reactions on Suspended Graphene: An Operando Kelvin Probe Force Microscopy Approach

Salma Khatun, Sidney R. Cohen, Sa'ar Shor Peled, Irit Rosenhek-Goldian, Robert S. Weatherup, Baran Eren*

S. Khatun, S. S. Peled, Dr. B. Eren
Department of Chemical and Biological Physics, Weizmann Institute of Science, 234 Herzl Street, 76100 Rehovot, Israel
E-mail: baran.eren@weizmann.ac.il

Dr. S. R. Cohen, Dr. I. Rosenhek-Goldian
Chemical Research Support, Weizmann Institute of Science, 234 Herzl Street, 76100 Rehovot, Israel

Prof. R. S. Weatherup
Department of Materials, University of Oxford, Parks Road, Oxford, Oxfordshire, OX1 3PH, United Kingdom

Keywords: suspended graphene, electrochemistry, Kelvin probe force microscopy, operando microscopy, graphene functionalization

Abstract: An electrochemical micro-reactor sealed with a single-layer graphene (SLG) membrane is demonstrated that allows straightforward measurement with established scanning probe microscopies. SLG serves as a working electrode which separates the liquid electrochemical environment from the ambient to enable direct energy-level determination. Kelvin probe force microscopy (KPFM) thereby reveals the shifts in Fermi-level of suspended SLG under electrochemical reaction conditions in aqueous alkaline media. Polymer-free transfer to create suspended SLG minimizes contributions to doping related to any support or contaminants, such that changes in work function (WF) relate predominantly to the electrochemical system under study. These WF changes are rationalized in the context of a simple model of electrochemical gating, providing insight into the interplay between electronic and electrochemical doping (through redox of water) of suspended graphene. Further changes in WF are attributable to the reversible

functionalization of graphene during the oxygen evolution reaction. Mechanical changes in the suspended graphene in the form of bulging also occur, which we attribute to electro-wetting of graphene induced by charge-carrier doping.

1. Introduction

Probing chemical and physical processes occurring at electrode-electrolyte interfaces at nm-scales promises new insights into electrochemical reactions intrinsic to sustainable energy storage and conversion technologies. A number of special approaches like scanning ion conductance microscopy and electrochemical scanning probe microscopy have been developed to spatially resolve structural or electronic information from the electrode-electrolyte interface.[1,2] However, these techniques do not yet approach the energy resolution that is achievable with established spectroscopic and microscopic techniques performed in ambient or vacuum conditions. Therefore, the method of capping a liquid-cell by a thin membrane, which is transparent to X-rays and/or electrons is now promoted as a means of examining phenomena occurring at the electrode-electrolyte interface. Graphene is often the membrane of choice, as it combines mechanical strength with single-atom thickness. Recently, reactor-cells developed with this graphene-membrane approach were shown to be feasible for characterizing materials in their reaction environment via electron microscopy and X-ray spectroscopy techniques.[3-10] However, graphene's high specific surface area makes it particularly susceptible to doping by its operating environment,[11] which may be influenced by its electromechanical behavior,[12,13] electrochemical reactions,[11] functionalization, as well as contamination during preparation of the reactor-cell,[14] including exposure to air.[15,16] Furthermore, the width of

the electrical double layer (EDL) formed in liquid environments can have a major influence on doping.[17,18]

Graphene's unique electronic structure, in which the valence and conduction bands touch at the K-point of the Brillouin zone (Dirac point, E_D) means that undoped graphene has a charge-carrier concentration close to zero.[19,20] This needs to be augmented for many applications of graphene-based devices, and thus a large body of literature exists on controllable doping of graphene. Electrostatic doping is prominently employed in field effect transistors (FET), where the charge-carrier concentration is controlled by varying the electric potential between graphene and a back-gate.[21-24] Electrochemical gating offers an alternative approach that has been verified using a combination of conductance and Raman spectroscopy measurements,[17,18] and in a number of cases may allow greater flexibility in tuning the charge-carrier density by changing the ion concentration in the solution. However, implementation of this concept requires knowledge and control of electrochemical reactions taking place on both graphene and other parts of the device.

In electrochemical gating, the gate is simply a counter-electrode (CE) in an electrochemical cell with graphene serving as the working-electrode (WE). The doping of graphene in this configuration follows the model suggested in ref.[17], which we go over in the Supporting Information (SI). In brief, a positive (negative) V_{WE} *vs* V_{CE} should induce hole (electron) doping that will shift E_F downwards (upwards), thereby leading to a higher (lower) work function (WF). The description we use here, which is doping of graphene, is essentially equivalent to the description used in ref.[14], which is electrolyte potential being altered by the dipole layer created at the EDL and unscreened potential being detected from above the surface. According to our model, approximately 125 meV shift in Fermi-level

(E_F) equivalent to roughly $10^{12}\cdot cm^{-2}$ doping can be estimated for a 10^{-3} M NaOH solution at ∓ 1 V using this model and assuming the EDL thickness to be equal to the Debye length (Figure S1, Supporting Information). This model, however, does not account for Faradaic processes. This is especially important for aqueous solutions as the thermodynamic stability window of water is only 1.23 V. At high anodic potentials where graphene is p-doped, the oxygen evolution reaction (OER) $4OH^- \rightarrow O_2 + 2H_2O + 4e^-$ *(graphene)* occurs supplying electrons and thus electrochemically lowering the extent of p-doping. Similarly, at high cathodic potentials graphene is n-doped, but the hydrogen evolution reaction (HER) $2H_2O + 2e^-$ *(graphene)* $\rightarrow H_2 + 2OH^-$ will extract electrons leading a lower extent of n-doping. Therefore, the magnitude of ΔWF should be smaller at higher anodic and cathodic potentials than what the electronic model predicts. Another Faradaic process that can potentially occur is the functionalization of graphene, which will inevitably change its WF.

The prevalent means of determining the level of doping and thereby the shifts in graphene's E_F is through Raman spectroscopy.[17,25] While this approach is well-established and easy to perform, it is an indirect method: It is difficult to unambiguously distinguish n- and p-type doping by the position of the Raman modes, which are further influenced by strain, defect density, and interactions with solvent.[26] Alternatively, conductance measurements are more direct, but the information obtained is typically averaged over a relatively large area. In order to test the validity of the doping model under practical conditions, we assembled an electrochemical reactor-cell and measured the WF of graphene directly with operando Kelvin probe force microscopy (KPFM). KPFM is a variant of atomic force microscopy (AFM) widely used to map nanoscale WF (surface potential for nonmetals) variations of surfaces in ambient or vacuum conditions.[27] This

could be of great importance for electrochemical systems, however, it is impractical in polar liquids due to screening and interference from surrounding fluid.[28,29] The graphene-membrane approach solves this problem, as graphene physically separates the scanning tip from the liquid environment.[14]

Several factors can shift graphene's E_F and must be carefully controlled for a proper analysis. We especially avoided two commonly used steps in our protocol that could lead to undesired artifacts. Firstly we studied suspended graphene regions to eliminate doping induced by the support-substrate either through charge transfer at the interface,[30] or interfacial reactions.[11,31,32] The second precaution was to avoid using a polymer material during transfer of graphene from its Cu growth substrate to the perforated support. Graphene is extremely lipophilic and polymer residues will inevitably change the WF of graphene. Despite claims that annealing or acetone cleaning remove such residues, contact-mode AFM measurements reveal a layer of such residues covering graphene even after such treatments.[33-35] Such treatments can also result in structural damage to the graphene.[36] There are only a handful of studies about the interaction of polymer-free, suspended graphene with liquids in the literature. In proof-of-concept studies in ref.[37], near-field infrared spectroscopy (another variant of AFM) was used to probe liquids beneath the graphene membrane. Another recent study showed that it is possible to measure the changes in the potential of graphene under electrochemical conditions using KPFM with a similar graphene-membrane approach.[14] However, this work employed bi-layer graphene (and SLG covered with nanoparticles) transferred with polymers that typically leave significant residues. This complicates analysis and introduces additional ambiguity in developing a model and is thus avoided here. The effects of the interface between

suspended graphene and water on the mechanical properties of graphene and on the electrical resistivity of graphene were also investigated recently,[12,13] but the preparation method involved the use of polymer in both of these studies as well. Another distinction of the work herein is that our suspended graphene regions were only 500 nm in diameter. This allowed for a stiffer membrane surface (stiffness varies linearly with diameter) and facilitated monitoring of 8-10 different such regions during the course of the experiment to observe statistical fluctuations.

In this work, we apply KPFM to study small enclosures of 500 nm diameter capped by single-layer graphene (SLG) membranes. The contact potential difference (CPD) between the scanning tip and these membranes or surrounding Au-supported graphene was measured at two different concentrations of sodium hydroxide (NaOH) solution (10^{-4} M and 10^{-3} M), as a function of voltage difference between the membrane and the CE. Topographical changes, mapped simultaneously with the CPD showed the effects of localized bubble formation due to gas evolution at the extreme cathodic and anodic potentials. In addition, the membrane height relative to the Au support varied when going from dry to wet conditions, with more subtle changes occurring as a function of applied potential. The consistency of measurements over many hours highlights the remarkable stability of the graphene membrane during scanning. In the context of the charge-carrier transfer model outlined above, we are able to rationalize the observed changes in CPD with voltage at the different ionic strengths, with deviations observed following high anodic potentials attributable to changes at the graphene surface due to electrochemical reactions.

2. Result and Discussions

Our sample has two regions: SLG on Au (30 nm) thin films (SLG/Au) supported by SiN_x, and suspended SLG. In the CPD results reported here, SLG/Au is used as the reference, and its WF is assumed not to change. In this way, any tip changes during the course of the scan do not affect the reported values. For the rest of the paper, the contrast in KPFM images will be referred to as CPD contrast ($\Delta CPD = CPD_{SLG} - CPD_{SLG/Au}$), with brighter CPD contrast corresponding to a lower local WF. Since WF of SLG/Au is held constant, ΔCPD values presented in our analysis are equivalent to $-\Delta WF_{SLG}$.

Under dry conditions, the suspended SLG is found to sag below the level of the SLG/Au regions (**Figure 1**a), with a height difference Δz ($z_{SLG}–z_{SLG/Au}$) of –5 to –20 nm. Upon addition of solution, Δz is notably reduced in magnitude (Figure 1). For instance, for the 10^{-3} M data set, $|\Delta z|$ is reduced from ~14.5 nm to ~6.5 nm (on average) upon the addition of liquid (Figure 1b) and from ~7 nm to ~4 nm (on average) for the 10^{-4} M data set. These changes cannot be attributed to significant pressure differentials as our single-reservoir configuration capped by the graphene sheet containing some defect regions would serve to relieve any pressure build-up. Rather, our observations (see below) suggest that the main reason for topographic changes is wetting. This change is always accompanied by a sharp change in phase contrast. The SLG/Au regions appear rougher than the unsupported SLG at tens of nanometer scale, due to the conformation of the SLG to the nanoscale grains of the evaporated Au thin film. For the dry system, the suspended SLG presents brighter CPD contrast than SLG/Au (Figure 1a), indicating it has a relatively lower WF. Given the suspended SLG has no substrate-induced doping, and contamination is minimized through the polymer-free preparation procedure and subsequent vacuum annealing to remove adsorbed hydrocarbons, E_F is assumed to be close to the Dirac point. On the other hand,

for the region SLG/Au, gold serves as a weakly-interacting metal that does not affect the linear dispersion of graphene's π-band close to E_D, but dopes graphene by charge transfer.[38,39] The higher WF observed for SLG/Au regions indicates a lower E_F and thus local p-doping, consistent with electrons from the graphene transferring to the Au that has high a WF.[40] The magnitude of the CPD contrast is about 30 mV. This contrast does not depend on applied voltage, confirming that the KPFM signal is not perturbed by the applied voltage when liquid electrolyte is not present.

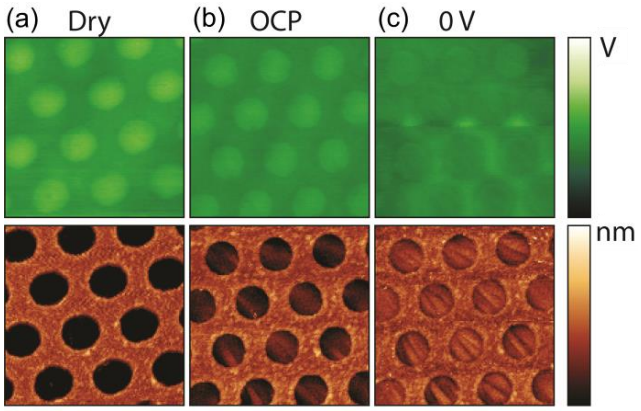


Figure 1. Comparison between the CPD and topography in dry and wet conditions, latter both at open circuit potential (OCP) and at 0 V. Example is at 10^{-3} M alkaline condition. Whilst CPD changes are within the experimental error, topographical changes are prominent. The color scale is 25 nm for the topography channel and 200 mV for the CPD channel.

On application of V_{WE} *vs* V_{CE} = 0 V, the apparent height difference between the unsupported and supported regions changes further: At 10^{-3} M, the suspended SLG regions become nearly level with the SLG/Au when 0 V is first applied (Figure 1c). At 10^{-4} M, no such change is initially observed and the height difference remains as ~4 nm. The CPD contrast at open-circuit potential (OCP), *i.e.*, prior to applying 0 V, slightly varies from that

of the dry system and that observed upon applying 0 V (Figure 1). However, these changes are small enough to be within the statistical error, and differ from sample to sample.

Images were then acquired at constant cathodic potentials down to V_{WE} *vs* V_{CE} = -1 V and constant anodic potentials up to V_{WE} *vs* V_{CE} = 1 V for the 10^{-3} M solution and with the window extended to ∓1.2 V for 10^{-4} M solution. This was repeated for several sweeps, with mapping of a representative sweep shown in **Figure 2**, and the Δz and ΔCPD data extracted from multiple sweeps summarized graphically in **Figure 3** and **Figure 4**. In Figures 3 and 4 each point consists of averages of line-profiles across all of the circular suspended SLG regions in images acquired at the specified experimental conditions, and analyzed to yield the sample mean and confidence intervals with 95% confidence calculated using Student's t-distribution (shown as the error bars in graphs). Complete measurement sets are presented in Figures S4-S5, Supporting Information. In the topography analysis of Figure 3, potential-dependent changes are apparent. At 10^{-4} M (Figure S4, Supporting Information), there are non-uniform changes in topography of different holes in the first cathodic sweep. This is seen at -0.4, -0.6, -0.8 V. In those images, some of the holes sag significantly, even deeper than for the dry state, whereas others bulge out and become level with the SLG/Au. This behavior results in the large statistical error seen for Figure 3a during the first sweep. At -1 V and -1.2 V the differences diminish and disappear, as all the holes bulged out almost equally. On the subsequent sweep to anodic voltages, first sagging is recovered, followed by a gradual transition between +0.2 V and +0.4 V from sagging to bulging. All of the holes remain bulged out for subsequent cathodic and anodic scans, except for the last scan in a new area where the holes appear slightly depressed at around 0 V, similar to the initial conditions. The mechanical behavior of the

suspended SLG at 10^{-3} M is similar (Figure S5, Supporting Information and 3b) to that at 10^{-4} M, with the noted difference that bulging occurs already at 0 V. At this molarity, the suspended graphene is always bulged at high anodic and cathodic potentials, but in some of the cathodic sweeps, it appears to sag around 0 V.

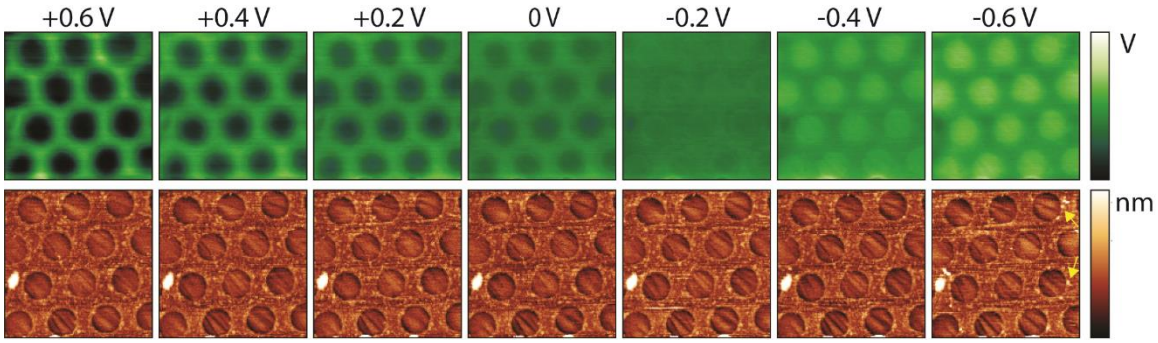


Figure 2. Example of some CPD and topography images obtained with our setup at various potentials with a NaOH solution with a molarity of 10^{-3} M. Imaging is from right to left (anodic sweep). The color scale is 25 nm for the topography channel and 200 mV for the CPD channel.

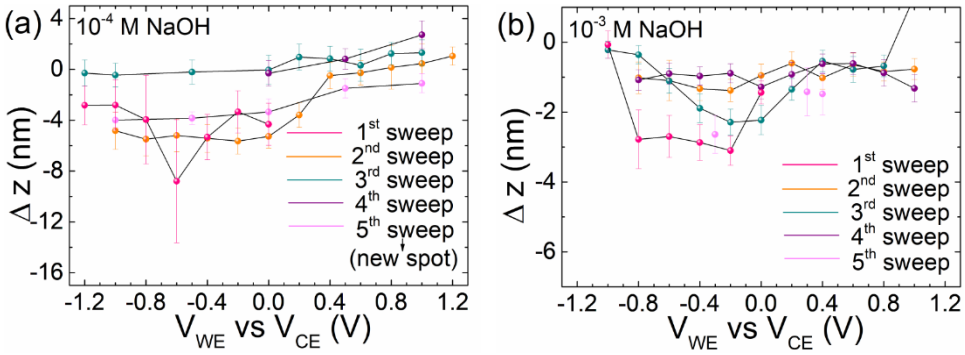


Figure 3. Variations in Δz (z_{SLG} -$z_{SLG/Au}$) as a function of the electrode potential for (a) 10^{-4} M and (b) 10^{-3} M. $z_{SLG/Au}$ is set as 0 nm reference height. Odd numbered sweeps are in cathodic direction; even numbered sweeps are in anodic direction.

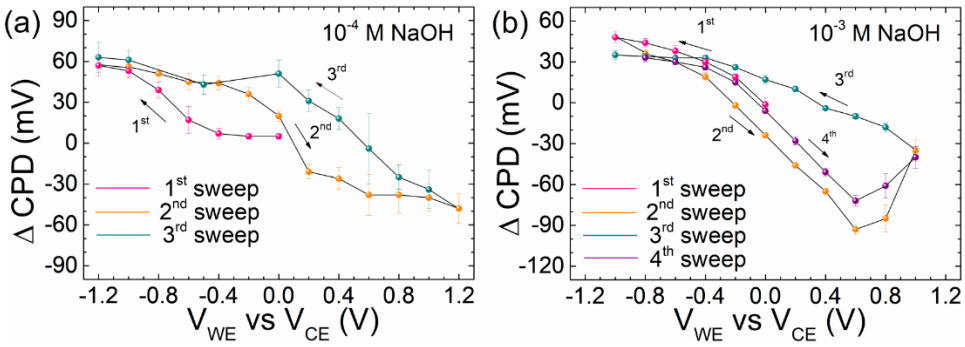


Figure 4. (a-b) Variations in ΔCPD as a function of the electrode potential measured using KPFM, for two different molarity values used. ΔCPD is defined as CPD_{SLG}-$CPD_{SLG/Au}$. Assuming $CPD_{SLG/Au}$ is constant, CPD_{SLG} is equal to change in the WF of graphene, or $-\Delta E_F/e$.

The observed graphene bulging cannot be simply attributed to excess gas formation, as it also happens at voltages within the water stability window. Moreover, there is no related CPD change corresponding to a loss of contact due to gas stuck between the liquid and SLG. Bulging of suspended graphene is commonly observed in STM imaging where the average tip-sample distance is lower compared to AFM imaging,[10] resulting in higher attractive interactions between the tip and the sample. However, there are only weak Van der Waals interactions in the present case and the electrostatic forces are nullified, therefore tip-sample interaction cannot explain the observed bulging. We verified this by increasing the size of the imaged frame, and do not observe any difference between previously imaged and freshly imaged regions (*e.g.*, last row of images in Figure S5). We therefore attribute these variations in the bulging of the graphene to electro-wetting behavior *i.e.*, changes in the graphene-water interaction with doping. Both experimental and theoretical studies suggest an increased wettability of hydrocarbon-free clean graphene with water, when graphene is either n-doped or p-doped.[41,42] For instance, the contact angle between graphene and water decreases from 88° to 78° when n-doped (-100 V polarization), and to

60° when p-doped (100 V polarization).[42] This, in turn, suggests a more pronounced decrease in the hydrophobicity of graphene for positive polarizations due to orientation of the water molecules. Our results are consistent with this, as bulging results from increased attractive interactions between graphene and the electrolyte solution at high potentials. In our experiments, slightly more pronounced bulging in molarity=10^{-3} M conditions compared to molarity=10^{-4} M conditions is consistent with the greater extent of doping.

In addition to bulging, further topographical changes are observed in the form of round protrusions (up to 100 nm diameter) on the SLG/Au areas, usually close the suspended SLG areas, when at high cathodic voltages (*e.g.*, -0.8 V and -1 V images in Figure S5, Supporting Information). Some of these protrusions fade away upon returning to less cathodic and then to anodic potentials, however some persist. Remnants of these can be seen in the image obtained at -0.6 V in Figure 2, marked with yellow arrows. We attribute these protrusions to the deformation of graphene due to formation of hydrogen gas, at the SLG/Au interface. This is similar to the electrochemical delamination of graphene that has been applied by a number of researchers as a means of transferring chemical vapor deposited graphene from conductive growth substrates.[43-45] These protrusions cause a localized change in CPD contrast, which could be related to the increase in graphene's WF with increasing strain.[46] However, such areas should not be included in the WF analysis since they are not representative of background or of SLG areas. We rarely observe these protrusions at high anodic potentials when oxygen gas forms.

As can be seen from the above discussion, by viewing the changes occurring over several different holes, we can distinguish different phenomena due to doping, electrochemical reactions, wettability, gas formation, and possible differences in the

graphene adherence around the hole perimeter. Imaging only a single hole carries the risk of observing non-representative behavior. We extend this approach in analysis to the results obtained in CPD channel, where the changes are more prominent than those we discussed in the topography channel. For instance, in the images shown in Figures 2, there is a contrast inversion in ΔCPD $(CPD_{SLG}\text{-}CPD_{SLG/Au})$ between cathodic voltages and anodic voltages. As discussed before, when we apply positive voltages, electrons will be drawn from the suspended SLG to the potentiostat and the E_F will be pushed down towards the valence band making the WF higher (Figure S1a). This results in the suspended SLG becoming relatively darker at anodic voltages. Similarly, at negative voltages electrons transferred from the potentiostat will dope the SLG, raising its E_F towards the conduction band and thus decreasing the WF (Figure S1a). In principle, as the potential is made more negative, the WF continues to decrease, *i.e.*, the suspended SLG will become even brighter. This reasoning provides a first-order explanation of the CPD changes in Figures 2 and S4-5, Supporting Information, but it must be modified due to electrochemical doping which counteracts the electronic doping. Figures 4a-b summarize the changes in ΔCPD from the first few scans of CPD contrast images in Figure S4-5, Supporting Information. If we compare the peak-to-peak values obtained at -1 V and 0.5 V (above 0.5 V is explained below), the experimental values are slightly lower than the predictions of the model shown in Figure S1b. This suggests the electrochemical doping via the redox reaction of water counteracts the electronic doping, as discussed in the introduction.

In both cases, there is a shift between the first scan and second scan. We believe this is due to initial electrochemical cleaning of graphene, as there is no repeatable pattern. A more interesting point is the increase in ΔCPD during the anodic scan above 0.6 eV for

molarity=10^{-3} M (Figure 4b). Here, OER most likely starts taking place, so this behavior could be related to electrochemical doping overcoming the electronic doping above 0.6 eV. We do not observe a similar behavior at cathodic voltages where hydrogen forms. We believe that there is a chemical effect during OER: the domain boundaries and defect sites of graphene are being functionalized with oxygen and hydroxides. This behavior above 0.6 eV also causes a hysteresis between the cathodic and anodic scans above 0 eV, because of the overpotentials in functionalization and de-functionalization. The phenomenon occurs repeatably, and is reversible. No systematic hysteresis exists in cathodic potentials, *i.e.*, de-functionalization happens roughly around 0 V, and no further changes happen at cathodic potentials. This is in line with electrochemical delamination experiments where changes take place under anodic potentials but not under cathodic potentials.[43-45] Such a hysteresis at anodic potentials was also observed in ref.[14] at molarity=10^{-1} M and it was attributed to oxidation of graphene to graphene oxide. We do not observe this behavior of sudden increase in ΔCPD at high anodic potential for molarity 10^{-4} M, consistent with the expected shift in the onset of OER to higher anodic potentials as the molarity decreases. There is however still some hysteresis at anodic voltages, suggesting graphene is still functionalized, although to a lesser extent. In line with the explanation of hysteretic behavior for molarity=10^{-3} M, CPD results at molarity=10^{-4} M also shows negligible hysteresis at cathodic voltages. We should also note that this functionalization would also change graphene's wetting properties quite significantly, making it even less hydrophobic.

To confirm the electrochemical cell was set up properly, we performed control experiments without the electrolyte and observed that both the topography and CPD remain unchanged when a potential is applied (Figure S6, Supporting Information).

In order to verify the functionalization of SLG at relatively high anodic potentials, we performed Raman spectroscopy measurements using the same setup. Whilst under OCP and initial cathodic potentials the Raman spectra exhibited the typical G and 2D peaks of SLG, without a significant D peak, under anodic potentials above 0.8 V the D peak grew in intensity and the 2D peak diminished (Figure S7, Supporting Information).This confirms functionalization of the graphene to form graphene oxide.[47.48] Upon reversing the potential to -1 V, the initial Raman spectrum of graphene was not recovered, and remained similar to that of graphene oxide. This means that after one oxidation and reduction cycle, the graphene should be considered as a 'reduced graphene oxide',[49] that is, graphene with a higher defect density. There is no noticeable difference in terms of the Fermi-level between graphene and reduced graphene oxide (Figure 4b).

To examine the effect of electrochemistry on the integrity of the SLG, we performed ex-situ scanning and transmission electron microscopy (SEM and TEM) measurements. Figures S8 and S9, Supporting Information, show examples of such images after the experiments at 10^{-4} M, which show no obvious signs of deterioration. The only notable change observed, is that in high-magnification TEM images Au nanoparticles are detectable near the edge of the suspended SLG region which were not there initially. However, their presence does not affect the CPD analysis above, as only the central region of the holes were considered. Measurement of the electrolyte's pH value before and after the experiments show no detectable change, confirming there is no significant loss of water during the experiment due to either gas formation or evaporation. It should also be noted that an imaging artifact is apparent in the CPD images of halos corresponding with the edges of the circular suspended SLG regions. These can be more readily distinguished at -

0.2 V in Figure 2 as the CPD contrast between the SLG and SLG/Au regions is low. These could arise from the Au nanoparticles seen in TEM, but given the change in topography at the edge of the suspended regions, we primarily attribute them to an increased interaction with the side of the scanning tip during the second pass (Kelvin) scan. Again, these do not influence the CPD analysis herein as only the central regions of the suspended SLG are considered.

One issue we sometimes encounter with our setup is the intercalation of the electrolyte solution between SLG and Au in certain regions, usually occurring abruptly when a bias is applied or changed. This results in spatial fluctuations in the reference CPD signal, sometimes accompanied by changes in topography due to intercalated water. We can readily detect such an event, and therefore refrain from using such data sets in this work. We can also exclude a thick, uniform layer of intercalated electrolyte solution, the result of which would be no spatial variation in CPD between holes and supported regions, because we always do have such variations and furthermore do not observe any bias-dependent variations in our phase contrast images which we have found to be sensitive to the surface supporting the graphene. However, we cannot exclude the intercalation of a thin layer of the electrolyte solution, e.g., a few atomic layers, due to electro-wetting. When this happens, CPD of both SLG and SLG/Au regions will become offset from their ideal values due to imperfect grounding of graphene (loss of contact to Au). We did not observe any effect of this on the ΔCPD trends as this effect would be relatively small and should assume the same offset for both regions.

3. Conclusions

The *ΔWF* trends we observe for suspended graphene in alkaline electrochemical conditions are reasonably well explained by the simple electronic doping model. Experimental values are lower than predicted values due to electrochemical doping (through redox reaction of water) counteracting the electronic doping. Deviation from this model is observed at high anodic potentials, which is attributable to the functionalization of graphene at potentials close to the onset of OER, but the predicted behavior is recovered on returning to cathodic potentials. Potential-dependent topographic changes in the suspended graphene are observed which are attributable to changes in graphene wettability with doping, *i.e.*, electro-wetting, as well as functionalization of graphene during OER. Graphene is observed to remain intact throughout numerous electrochemical cycles, and bursting of the membranes was never observed under the conditions used herein. The experimental approach and results presented here serve as a benchmark for future studies of the electrochemical behavior of two-dimensional materials both in aqueous and organic electrolytes, and the underlying mechanisms of doping.

4. Experimental Section

Sample Preparation: SLG-membranes were prepared following the procedure outlined in ref.[10]. Briefly, chemical vapor deposited (CVD) SLG on polycrystalline Cu foil was transferred onto Au-coated SiN_x grids containing an array of perforated holes of 500 nm diameter. A polymer-free transfer was used to avoid polymer residues that would otherwise influence the WF of graphene. The samples were also annealed in ultra-high vacuum (UHV) at 300 °C for 4 h prior to the KPFM measurements in order to desorb atmospheric contaminants that change the WF and wettability of graphene.[15,16] We do not

observe any CPD contrast between SLG and SLG/Au regions in dry conditions if the sample was not annealed.

E-beam evaporation of Au (30 nm) onto the SiN_x grids prior to transfer ensures electrical connectivity to the SLG over large areas, even in the presence of small SLG cracks induced by the transfer process. A Cr 3 nm layer was deposited prior to Au, in order to increase the adhesion of Au and avoid delamination during experiments. More details of the preparation methods and schematic diagram (Figure S2, Supporting Information) are available in the Supporting Information. Characterization of our samples by multiple techniques including scanning and transmission electron microscopies (SEM and TEM), Raman spectroscopy, and AFM (Figure S3, Supporting Information) are shown in the Supporting Information.

Electrochemical setup: For electrochemical experiments, a custom-built two-electrode cell accommodates a SLG membrane as WE, with a Pt wire serving as both CE and quasi-reference electrode (RE), as shown in Figure S10a, Supporting Information. This cell contains a liquid reservoir within its polyether ether ketone (PEEK) housing that is sealed with the SLG membrane (3 mm diameter SiN_x grid) sandwiched between a perfluoroelastomer O-ring and stainless steel lid, which has a 2 mm aperture. We used mildly alkaline aqueous (molarity of 10^{-4} and 10^{-3} M) NaOH solution in our KPFM measurements. Prior to the AFM studies, cyclic voltammetry (CV) measurements were done with a scan-rate of 0.02 V/sec. Figure S10b, Supporting Information, shows the voltammogram obtained when a molarity of 10^{-4} M was used. The stability window of water can be clearly seen. There are some subtle features at around 0.1 V in the cathodic scan and at around 0.8 V in the anodic scan. With an ensemble technique like CV, it is not

possible to distinguish between features related to graphene from those related to the underlying Au layer, although the nominal surface area of Au is four times lower than that of graphene. For instance, similar peaks were observed in electrochemical studies on Au in alkaline aqueous solutions.[50-52] Direct comparison of the potentials measured with our system to values reported in literature is not possible because the two-electrode configuration leads to shifts in the redox potentials.

KPFM measurements: With KPFM, localized information can be obtained for SLG regions that is not available with ensemble techniques like CV, where the signal is averaged over all parts of the reactor-cell. KPFM measurements were performed using amplitude modulation (AM-AFM and AM-KPFM) with a NTEGRA AFM (from NT-MDT) in double-pass scanning mode: First, the topography of each fast-scan line is recorded using intermittent-contact mode for distance control. The free oscillation amplitude (A_0) was 50-75 nm and a typical setpoint oscillation amplitude (A_{sp}) of around $0.8 \cdot A_0$ was chosen for distance-control feedback. This setpoint ratio was found to give a clear contrast in the phase signal between dry and wet conditions, which we used to verify contact with the underlying liquid. Higher setpoint ratios (lower tapping force) did not give such contrast. CPD was measured in a second pass of each scan line at a constant distance from the sample (lift height = 10–14 nm). The electrostatically excited amplitude during the Kelvin measurement was under 10 nm. The frequency of the applied electrical modulation was matched to the first flexural frequency of the cantilever, and the Kelvin controller cancels electrostatic forces by adjusting the tip bias voltage, V_{dc}, until zero amplitude is reached.[27,29] Here, V_{dc} compensates for the potential difference between the tip and the

sample, hence $V_{dc} = V_{cpd}$ and $WF_{sample} = WF_{tip} - eV_{dc}$. The local variations of the WF along the x and y direction can be expressed as $\Delta WF_{sample} = -e\Delta V_{dc}$.

It has been suggested that a geometry-dependent contribution from the cantilever can influence the CPD values obtained above a small feature. [53] We took several precautions to minimize this effect: First of all, the cantilever of the probe used (Olympus AC240) is tapered at the end so the cantilever area above the tip is minimized. Secondly, the tip is positioned at the very end of the cantilever so that the contribution of the cantilever is reduced, and asymmetric. The latter feature should lead to different contrast at the bottom relative to the top of the circular features in the CPD image, but this was not observed, indicating that overall there is not a strong cantilever influence. We also used small lift heights (smaller than those used in the simulations in ref.[53]) to enhance the tip contribution. Finally, we have made measurements on grids of different sizes (500 nm diameter and 1 μm diameter). There is no difference in the ΔCPD measured on these two different-sized grids indicating conclusively that under our conditions there is no significant effect of contrast lowering by the influence of the cantilever. Nevertheless, we cannot fully exclude the possibility that AM-KPFM mode slightly underestimates the ΔCPD due to averaging effects.[54]

Reported results represent a minimum of two different samples measured on different days.

Supporting Information

Supporting Information is available from the Wiley Online Library or from the author.

Acknowledgements

We are grateful to Dr. Ifat Kaplan-Ashiri, Dr. Olga Brontvein, and Dr. Iddo Pinkas

from the Chemical Research Unit of the Weizmann Institute of Science for the electron microscopy images and the Raman spectra. This research is supported by the Weizmann – UK Making Connections Programme and the Minerva Foundation with funding from the Federal German Ministry for Education and Research. SK acknowledges the VATAT fellowships for international visiting students and CSIR Fellowship No.09/080(1054)/2017-EMR-I (Roll No. 523092). BE acknowledges the support from the Zuckerman STEM Leadership Faculty Fellowship.

References

[1] A. Page, D. Perry, P. R. Unwin, *Proc. R. Soc. A-Math. Phys. Eng. Sci.* **2017**, *473*.

[2] Y. C. Hang, J. H. K. Pfisterer, D. McLaughlin, C. Csoklich, L. Seidl, A. S. Bandarenka, O. Schneider, *Small Methods* **2019**, *3*, 1800387.

[3] M. Krueger, S. Berg, D. Stone, E. Strelcov, D. A. Dikin, J. Kim, L. J. Cote, J. X. Huang, A. Kolmakov, *ACS Nano* **2011**, *5*, 10047.

[4] J. M. Yuk, J. Park, P. Ercius, K. Kim, D. J. Hellebusch, M. F. Crommie, J. Y. Lee, A. Zettl, A. P. Alivisatos, *Science* **2012**, *336*, 61.

[5] C. H. Wang, Q. Qiao, T. Shokuhfar, R. F. Klie, *Adv. Mater.* **2014**, *26*, 3410.

[6] J. Park, H. Elmlund, P. Ercius, J. M. Yuk, D. T. Limmer, Q. Chen, K. Kim, S. H. Han, D. A. Weitz, A. Zettl, A. P. Alivisatos, *Science* **2015**, *349*, 290.

[7] J. Park, H. Park, P. Ercius, A. F. Pegoraro, C. Xu, J. W. Kim, S. H. Han, D. A. Weitz, *Nano Lett.* **2015**, *15*, 4737.

[8] A. Kolmakov, D. A. Dikin, L. J. Cote, J. X. Huang, M. K. Abyaneh, M. Amati, L. Gregoratti, S. Gunther, M. Kiskinova, *Nat. Nanotechnol.* **2011**, *6*, 651.

[9] C. H. Wu, R. S. Weatherup, M. B. Salmeron, *Phys. Chem. Chem. Phys.* **2015**, *17*, 30229.

[10] R. S. Weatherup, B. Eren, Y. B. Hao, H. Bluhm, M. B. Salmeron, *J. Phys. Chem. Lett.* **2016**, *7*, 1622.

[11] H. Pinto, A. Markevich, *Beilstein J. Nanotechnol.* **2014**, *5*, 1842.

[12] G. A. Ferrari, A. B. de Oliveira, L. Silvestre, M. J. S. Matos, R. J. C. Batista, T. F. D. Fernandes, L. M. Meireles, G. S. N. Eliel, H. Chacham, B. R. A. Neves, R. G. Lacerda, *ACS Nano* **2018**, *12*, 4312.

[13] L. M. Meireles, E. G. S. Neto, G. A. Ferrari, P. A. A. Neves, A. C. Gadelha, I. Silvestre, T. Taniguchi, K. Watanabe, H. Chacham, B. R. A. Neves, L. C. Campos, R. C. Lacerda, *Adv. Electron. Mater.* **2020**, *6*, 1901167.

[14] E. Strelcov, C. Arble, H. X. Guo, B. D. Hoskins, A. Yulaev, I. V. Vlassiouk, N. B. Zhitenev, A. Tselev, A. Kolmakov, *Nano Lett.* **2020**, *20*, 1336.

[15] D. Martinez-Martin, R. Longuinhos, J. G. Izquierdo, A. Marele, S. S. Alexandre, M. Jaafar, J. M. Gomez-Rodriguez, L. Banares, J. M. Soler, J. Gomez-Herrero, *Carbon* **2013**, *61*, 33.

[16] A. I. Aria, P. R. Kidambi, R. S. Weatherup, L. Xiao, J. A. Williams, S. Hofmann, *J. Phys. Chem. C* **2016**, *120*, 2215.

[17] A. Das, S. Pisana, B. Chakraborty, S. Piscanec, S. K. Saha, U. V. Waghmare, K. S. Novoselov, H. R. Krishnamurthy, A. K. Geim, A. C. Ferrari, A. K. Sood, *Nat. Nanotechnol.* **2008**, *3*, 210.

[18] F. Chen, Q. Qing, J. L. Xia, J. H. Li, N. J. Tao, *J. Am. Chem. Soc.* **2009**, *131*, 9908.

[19] P. R. Wallace, *Phys. Rev.* **1947**, *71*, 622.

[20] A. H. Castro Neto, F. Guinea, N. M. R. Peres, K. S. Novoselov, A. K. Geim, *Rev. Mod. Phys.* **2009**, *81*, 109.

[21] K. S. Novoselov, A. K. Geim, S. V. Morozov, D. Jiang, Y. Zhang, S. V. Dubonos, I. V. Grigorieva, A. A. Firsov, *Science* **2004**, *306*, 666.

[22] K. S. Novoselov, A. K. Geim, S. V. Morozov, D. Jiang, M. I. Katsnelson, I. V. Grigorieva, S. V. Dubonos, A. A. Firsov, *Nature* **2005**, *438*, 197.

[23] Y. B. Zhang, Y. W. Tan, H. L. Stormer, P. Kim, *Nature* **2005**, *438*, 201.

[24] D. Reddy, L. F. Register, G. D. Carpenter, S. K. Banerjee, *J. Phys. D-Appl. Phys.* **2011**, *44*.

[25] A. C. Ferrari, D. M. Basko, *Nat. Nanotechnol.* **2013**, *8*, 235.

[26] J. E. Lee, G. Ahn, J. Shim, Y. S. Lee, S. Ryu, *Nat. Commun.* **2012**, *3*, 1024.

[27] M. Nonnenmacher, M. P. Oboyle, H. K. Wickramasinghe, *Appl. Phys. Lett.* **1991**, *58*, 2921.

[28] L. Collins, S. Jesse, J. I. Kilpatrick, A. Tselev, M. B. Okatan, S. V. Kalinin, B. J. Rodriguez, *Beilstein J. Nanotechnol.* **2015**, *6*, 201.

[29] L. Collins, S. A. L. Weber, B. J. Rodriguez, in *Kelvin Probe Force Microscopy* (Eds: Sadewasser S.; T. Glatzel), Springer International Publishing AG, **2018**, p. 391-433.

[30] G. Giovannetti, P. A. Khomyakov, G. Brocks, V. M. Karpan, J. van den Brink, P. J. Kelly, *Phys. Rev. Lett.* **2008**, *101*, 026803.

[31] P. L. Levesque, S. S. Sabri, C. M. Aguirre, J. Guillemette, M. Siaj, P. Desjardins, T. Szkopek, R. Martel, *Nano Lett.* **2011**, *11*, 132.

[32] H. Xu, Y. B. Chen, J. Zhang, H. L. Zhang, *Small* **2012**, *8*, 2833.

[33] A. M. Goossens, V. E. Calado, A. Barreiro, K. Watanabe, T. Taniguchi, L. M. K. Vandersypen, *Appl. Phys. Lett.* **2012**, *100*, 073110.

[34] N. Lindvall, A. Kalabukhov, A. Yurgens, *J. Appl. Phys.* **2012**, *111*, 064904.

[35] G. Fessler, B. Eren, U. Gysin, T. Glatzel, E. Meyer, *Appl. Phys. Lett.* **2014**, *104*, 041910.

[36] M. Kratzer, B. C. Bayer, P. R. Kidambi, A. Matkovic, R. Gajic, A. Cabrero-Vilatela, R. S. Weatherup, S. Hofmann, C. Teichert, *Appl. Phys. Lett.* **2015**, *106*.

[37] Y. H. Lu, J. M. Larson, A. Baskin, X. Zhao, P. D. Ashby, D. Prendergast, H. A. Bechtel, R. Kostecki, M. Salmeron, *Nano Lett.* **2019**, *19*, 5388.

[38] A. Dahal, M. Batzill, *Nanoscale* **2014**, *6*, 2548.

[39] R. S. Weatherup, L. D'Arsie, A. Cabrero-Vilatela, S. Caneva, R. Blume, J. Robertson, R. Schloegl, S. Hofmann, *J. Am. Chem. Soc.* **2015**, *137*, 14358.

[40] Electron Work Function of the Elements, CRC Handbook of Chemistry and Physics, 97th edition; CRC Press, 2016; pp. 12–123.

[41] T. Tian, S. C. Lin, S. Y. Li, L. L. Zhao, E. J. G. Santos, C. J. Shih, *Langmuir* **2017**, *33*, 12827.

[42] G. Hong, Y. Han, T. M. Schutzius, Y. M. Wang, Y. Pan, M. Hu, J. S. Jie, C. S. Sharma, U. Muller, D. Poulikakos, *Nano Lett.* **2016**, *16*, 4447.

[43] Y. Wang, Y. Zheng, X. F. Xu, E. Dubuisson, Q. L. Bao, J. Lu, K. P. Loh, *ACS Nano* **2011**, *5*, 9927.

[44] L. B. Gao, W. C. Ren, H. L. Xu, L. Jin, Z. X. Wang, T. Ma, L. P. Ma, Z. Y. Zhang, Q. Fu, L. M. Peng, X. H. Bao, H. M. Cheng, *Nat. Commun.* **2012**, *3*, 699.

[45] R. S. Weatherup, A. J. Shahan, Z. J. Wang, K. Mingard, A. J. Pollard, M. G. Willinger, R. Schloegl, P. W. Voorhees, S. Hofmann, *Nano Lett.* **2016**, *16*, 6196.

[46] A. Volodin, C. Van Haesendonck, O. Leenaerts, B. Partoens, F. M. Peeters, *Appl. Phys. Lett.* **2017**, *110*, 193101.

[47] K. N. Kudin, B. Ozbas, H. C. Schniepp, R. K. Prud'homme, I. A. Aksay, R. Car, *Nano Lett.* **2008**, *8*, 36.

[48] K. Krishnamoorthy, M. Veerapandian, K. Yun, S. J. Kim, *Carbon* **2013**, *53*, 38.

[49] N. M. S. Hidayah, W. W. Liu, C. W. Lai, Z. Noriman, C. S. Khe, U. Hashim, H. C. Lee, *AIP Conference Proceedings*, **2017,** 1892, 150002.

[50] A. Hamelin, M. J. Sottomayor, F. Silva, S. C. Chang, M. J. Weaver, *J. Electroanal. Chem.* **1990**, *295*, 291.

[51] M. M. Jaksic, B. Johansen, R. Tunold, *Int. J. Hydrog. Energy* **1993**, *18*, 91.

[52] R. L. Doyle, M. E. G. Lyons, *J. Solid State Electrochem.* **2014**, *18*, 3271.

[53] H.O. Jacobs, P. Leuchtmann, O.J. Homan, A. Stemmer, *J. Appl. Phys.* **1998**, *84*, 1168.

[54] Th. Glatzel, S. Sadewasser, M.Ch. Lux-Steiner, *Appl. Surf. Sci*. **2003**, *210*, 84.

ToC

Sketch of the electrochemical cell capped with a single layer graphene for operando KPFM measurements is shown in the left. The simple electronic doping model shown in the middle is a good first-order approximation, as verified by the images in right: Work function of graphene changes depending on polarization. Chemical reactions result in deviations from this model.

S. Khatun 1, S. R. Cohen 2, S. S. Peled 1, I. R. Goldian 2, R. S. Weatherup 3, B. Eren* 1

Observing Electrochemical Reactions on Suspended Graphene: An Operando Kelvin Probe Force Microscopy Approach

